



Enhancement of SAR Speckle Denoising Using the Improved Iterative Filter

Mohamed Yahia, Tarig Ali, Mohammad Mortula, Riadh Abdelfattah, Samy Mahdy, Nuwanthi Arampola

► To cite this version:

Mohamed Yahia, Tarig Ali, Mohammad Mortula, Riadh Abdelfattah, Samy Mahdy, et al.. Enhancement of SAR Speckle Denoising Using the Improved Iterative Filter. IEEE Journal of Selected Topics in Applied Earth Observations and Remote Sensing, 2020, 13, pp.859 - 871. 10.1109/js-tars.2020.2973920 . hal-03586035

HAL Id: hal-03586035

<https://imt-atlantique.hal.science/hal-03586035>

Submitted on 23 Feb 2022


HAL is a multi-disciplinary open access archive for the deposit and dissemination of scientific research documents, whether they are published or not. The documents may come from teaching and research institutions in France or abroad, or from public or private research centers.

L'archive ouverte pluridisciplinaire **HAL**, est destinée au dépôt et à la diffusion de documents scientifiques de niveau recherche, publiés ou non, émanant des établissements d'enseignement et de recherche français ou étrangers, des laboratoires publics ou privés.



Distributed under a Creative Commons Attribution 4.0 International License

Enhancement of SAR Speckle Denoising Using the Improved Iterative Filter

Mohamed Yahia , Tarig Ali , Mohammad Maruf Mortula , Riadh Abdelfattah, *Senior Member, IEEE*, Samy El Mahdy, and Nuwanthi Sashipraba Arampola

Abstract—The recent advancement in synthetic aperture radar (SAR) technology has enabled high-resolution imaging capability that calls for efficient speckle filtering algorithms to preprocess radar imagery. Since the introduction of the Lee sigma filter in 1980, the various versions of the minimum mean square error (MMSE) filter were developed, focusing essentially on how to estimate the processed pixels. For instance, the iterative MMSE (IMMSE) filter that is commonly initialized by the boxcar filter maintains the initially filtered homogeneous areas and corrects the initially blurred spatial details after a few iterations. In this article, an effort is made to enhance the performance of the IMMSE filter in terms of speckle reduction and spatial detail preservation by refining the choice of the initial filter, optimizing its parameters, and improving the estimation of local statistics. Compared with the basic version, results showed that the improved iterative filter considerably enhanced the filtering criteria. When the improved iterative filtering process was initialized by the nonlocal mean filter, for few iterations, the filtering performances were improved. Simulated, airborne (ESAR, Oberpfaffenhofen Germany) and spaceborne (Sentinel 1, Palm Jumeirah Dubai UAE) SAR data were used to assess the filtering performances of the studied filters.

Index Terms—Iterative minimum mean square error (IMMSE) filter, nonlocal means filter, synthetic aperture radar (SAR), speckle.

I. INTRODUCTION

THE synthetic aperture radar (SAR) presents many benefits over optical remote sensing [1], principally the all-day and all-weather acquisition capability. SAR images have been used for a wide range of applications, such as disaster monitoring and forestry, agriculture. However, SAR images are affected by

the multiplicative speckle noise, which degrades its radiometric quality and reduces the performances of information extraction techniques. For these reasons, several methods have been introduced to reduce speckle. Such methods, however, need to carefully avoid spoiling useful information in the images, such as a local mean of backscatter, point targets, and textures.

The multilooking process reduces speckle in SAR images by averaging the intensities of neighboring pixels [2]. The major drawback of this method is the degradation of the spatial resolution. Many other despeckling filters have been developed to avoid this deficiency to a certain degree by using different estimation domains, including spatial [3], wavelet [4], and homomorphic wavelet [5], [6].

Nonlocal (NL) means filtering is one of the patch-based methods, where the pixel selection for filtering can be outstretched to the global neighborhood instead of restricting the local filtering window [7]. In fact, the main idea here is forming a local convolution mask, where each pixel value is proportional to the similarity between the central and each of the off-central pixels. Such similarity has been estimated using a number of approaches, among them, is the Euclidean distance [7]. Zhong *et al.* [8] applied the NL means (NLM) to filter SAR images by adapting the use of Euclidean distance to multiplicative noise. Recently, Vitale *et al.* [9] proposed an NL SAR despeckling filter that makes use of optical imagery. The probabilistic-patch-based filter aimed to introduce a suitable patch-based weight to generalize the Euclidean-distance-based weight used in the NLM algorithm [10]. These filters improved significantly the filtering performance of SAR images. However, they present the disadvantage of huge complexity and high computing cost.

The total-variation-based methods [11] have been extensively applied for SAR image speckle reduction due to their efficiency and the ability to preserve spatial details. Wavelet-based algorithms [4], as well as the methods based on the second-generation wavelets [12], bandelets [13], shearlet [14], etc., constituted an important group of speckle filtering techniques. With increased complexity, these techniques provided better spatial detail preservation; however, artifacts can be generated. Furthermore, these techniques apply the logarithmic transform to SAR images data so that noise became additive. A bias-compensation step is necessary to correct the non-Gaussianity in log-space. Also, several techniques based on a Bayesian NL framework have been developed for denoising SAR images [15]. The NL principle has been successfully used to despeckle in the wavelet domain [16], [17]. Martino *et al.* [18] extended the block

Manuscript received September 1, 2019; revised November 23, 2019 and January 15, 2020; accepted February 11, 2020. Date of publication February 24, 2020; date of current version March 17, 2020. This work was supported by Smart City Research Institute Grant from the American University of Sharjah, UAE under Grants EN0-282 and EN0-284. (Corresponding author: Mohamed Yahia.)

Mohamed Yahia is with the GIS and Mapping Laboratory, American University of Sharjah, Sharjah 26666, UAE, and also with the Laboratoire de recherche Modélisation analyse et commande de systèmes- MACS, Ecole Nationale d'Ingénieurs de Gabes - 6023 ENIG, Université de Gabes Tunisia, Tunis 1068, Tunisia (e-mail: myahya@aus.edu).

Tarig Ali, Samy El Mahdy, and Nuwanthi Sashipraba Arampola are with the GIS and Mapping Laboratory, American University of Sharjah, Sharjah 26666, UAE (e-mail: atarig@aus.edu; selmahdy@aus.edu; aarampola@aus.edu).

Mohammad Maruf Mortula is with the Civil Engineering Department, American University of Sharjah, Sharjah 26666, UAE (e-mail: mmortula@aus.edu).

Riadh Abdelfattah is with the COSIM Laboratory, Higher School of Communications of Tunis, University of Carthage, Ariana 2083, Tunisia, and also with the Département ITI, Télécom Bretagne, Institut de Télécom, Brest 29238, France (e-mail: riadh.abdelfattah@supcom.tn).

Digital Object Identifier 10.1109/JSTARS.2020.2973920

matching three-dimensional filter by representing the similarity measure among blocks of pixels according to Zhao *et al.* [11]. Recently, Penna *et al.* addressed the NLM filtering by replacing the Euclidean distance with stochastic distances in the Haar wavelet domain [19].

The IDAN filter [20] was introduced as an adaptive technique based on local stationary assumption. A “window growing” technique has been employed to constitute an adaptive neighborhood for each pixel with an aggregation test that combines the available intensity component information in order to measure the similarity between the central and off-center pixels.

The minimum mean square error (MMSE)-based filters that account for the local statistics of the image have been broadly applied in SAR speckle filtering. Since the introduction of the Lee sigma filter in early 1980 [21], [22], many enhanced versions have been proposed in the literature, such as Kuan [23], Frost [24], and the improved Lee [25], [26]. Many of these speckle filters have been implemented in GIS and remote sensing software due to their effectiveness in speckle reduction, simplicity, and low computational demand. The MMSE estimation is switched by maximum *a posteriori* [27], [28].

An iterative MMSE (IMMSE) filter has been introduced [29], [30]. The IMMSE filter is commonly initialized by the boxcar filter. Then, after a few iterations, the IMMSE method maintains the filtered homogeneous areas and corrects the initially blurred spatial details. Hamrouni *et al.* extended the use of the IMMSE to polarimetric SAR (PolSAR) images [31].

In this article, an effort is made to enhance the performance of the IMMSE filter. The improvements consisted in the choice of the initially filtered image, the parameter optimizing, and the estimation of the local statistics.

The rest of this article is organized as follows. Section II reviews the related work and then presents the proposed improved iterative filter. The results and discussions are shown in Section III. Finally, Section IV concludes this article.

II. RELATED WORK, MOTIVATIONS, AND PROPOSED FILTER

A. Related Work

The principle of spatial-domain SAR speckle filtering procedures includes the following.

- 1) The selection of homogeneous pixels.
- 2) The estimation of the filtered pixel value within the selected pixels.

The main methods that have been used for the second step are mean averaging, median, and MMSE [2], [7]–[8], [20]–[31]. In this article, a new formulation of the IMMSE filter is proposed.

The intensity pixel $y(i)$ of a SAR image is affected by a multiplicative noise [2]

$$y(i) = x(i) \nu(i) \quad (1)$$

where $x(i)$ is the noise-free pixel, and $\nu(i)$ is the speckle noise with unit mean and standard deviation σ_ν . The objectives of SAR speckle filtering are

- 1) reduce speckle in extended homogeneous areas. The optimal scenario is to average all pixels (i.e., $\hat{x}(i) = \bar{y}(i)$),

- 2) retain the spatial details in structured areas. The filtered pixel $\hat{x}(i)$ should maintain the value of the original pixel (i.e., $\hat{x}(i) = y(i)$).

In general, a filtered pixel verifies

$$\hat{x}(i) \in [y(i), \bar{y}(i)] \text{ or } \hat{x}(i) \in [\bar{y}(i), y(i)] \quad (2)$$

considering that the pixel intensity $y(i)$ may be higher or lower to the local mean. In the rest of this article, only $\hat{x}(i) \in [\bar{y}(i), y(i)]$ will be written.

In the MMSE filters [21], [22], [25], [26], the filtered pixel $\hat{x}(i)$ is expressed as

$$\hat{x}(i) = \bar{y}(i) + b(i) (y(i) - \bar{y}(i)) \quad (3)$$

where

$$b(i) = \frac{\text{var}(x(i))}{\text{var}(y(i))} \quad (4)$$

and

$$\text{var}(x(i)) = \frac{(\text{var}(y(i)) - \bar{y}^2(i)\sigma_\nu^2)}{(1 + \sigma_\nu^2)} \quad (5)$$

where $\bar{y}(i)$ and $\text{var}(y(i))$ were the mean and the variance of $y(i)$, respectively. In practice, the parameter b can have negative values. In these cases, it is set to zero.

In homogeneous areas, $b(i) = 0$, so $\hat{x}(i) = \bar{y}(i)$, whereas in heterogeneous areas (e.g., point target), $b(i) = 1$ and $\hat{x}(i) = y(i)$. Generally, $0 < b(i) < 1$ and $\hat{x}(i) \in [\bar{y}(i), y(i)]$.

B. Motivations and the Proposed Improved Iterative Filter

The essence of the IMMSE method is to scan the dynamic range of $\hat{x}(i)$ in $[y(i), \bar{y}(i)]$ by the following iterative filtering procedure [29]–[31]:

$$\hat{x}_0(i) = \bar{y}(i), \quad (6)$$

$$\hat{x}_{k+1}(i) = \hat{x}_k(i) + b'_k(i) (y(i) - \hat{x}_k(i)). \quad (7)$$

If $0 < b'_k(i) < 1$, then $\hat{x}_\infty(i) = y(i)$ [since $y(i)$ is the solution of (7)] and $\hat{x}_k(i) \in [\bar{y}(i), y(i)]$ (see Appendix). The performance of the IMMSE filter depends on the choice of the initial filtered image \hat{x}_0 , the choice of the parameter $b'_k(i)$, and the precise estimation of the local statistics to compute $b'_k(i)$. This article contributes to the improvement of the basic IMMSE filter as described below.

1) *Choice of Initial Filtered Image \hat{x}_0* : Since the speckle reduction level of the IMMSE filter does not surpass that of the original filter [29]–[31], the initial filter must ensure a very high speckle reduction level. However, when spatial details are extremely blurred, the IMMSE filter requires more iterations to recover the spatial information, which reduced the speckle filtering level in homogeneous areas. In [29]–[31], the boxcar filter is utilized as an initial filter (i.e., $\hat{x}_0(i) = \bar{y}(i)$). In this article, the NLM has been implemented as initially applied filter.

2) *Choice of the Parameter $b'_k(i)$* : In the IMMSE filter, the key parameter was $b'_k(i)$. In fact, this parameter controls the performance of the filtering process as the parameter $b(i)$ in (3). Hence, and in order to ensure robust speckle filtering,

this parameter must demonstrate the following three important properties:

- 1) $0 < b'_k(i) < 1$ unless, $\hat{x}_\infty(i) \neq y(i)$ and $\hat{x}_k(i) \notin [\bar{y}(i), y(i)]$ (see Appendix),
- 2) $b'_k(i) \approx 0$ in homogeneous areas,
- 3) $b'_k(i) \approx 1$ in heterogeneous areas.

Hence, by running few iterations (i.e., N iterations), the proposed filtering process maintained the filtered homogeneous areas (i.e., $\hat{x}_N(i) = \bar{y}(i)$ since $b'_k(i) \approx 0$) and preserved spatial details (i.e., $\hat{x}_N(i) = y(i)$ since $b'_k(i) \approx 1$).

By combining (4) and (5), we have

$$b(i) = \frac{\text{var}(x(i))}{((1 + \sigma_v^2)\text{var}(x(i)) + \bar{y}^2(i)\sigma_v^2)}. \quad (8)$$

In [29] and [31], $x(i)$ is substituted by its estimate $\hat{x}_1(i)$ and $\bar{y}(i)$ by $\hat{x}_0(i)$. Then, an empirical expression of the parameter $b'_k(i)$ was given by

$$b'_k(i) = \frac{\text{var}(\hat{x}_k(i))}{((1 + \sigma_v^2)\text{var}(\hat{x}_k(i)) + \hat{x}_k^2(i)\sigma_v^2)}. \quad (9)$$

In [30], a theoretic expression analog to (9) is developed. In practice, unlike the parameter $b(i)$ in (2), it can be seen that $0 < b'_k(i) < 1$. For one look image, expression (9) can be written as follows:

$$b'_k(i) = \frac{\frac{\text{var}(\hat{x}_k(i))}{\hat{x}_k^2(i)}}{\left(2\frac{\text{var}(\hat{x}_k(i))}{\hat{x}_k^2(i)} + 1\right)}. \quad (10)$$

By substituting $\hat{x}_k(i)$ by its mean $\bar{\hat{x}}_k(i)$, the new expression become

$$b'_k(i) = \frac{CV_{\hat{x}_k}^2(i)}{(2CV_{\hat{x}_k}^2(i) + 1)} \quad (11)$$

where

$$CV_{\hat{x}_k}(i) = \frac{\text{std}(\hat{x}_k(i))}{\bar{\hat{x}}_k} \quad (12)$$

where $\text{std}()$ is the standard deviation. Hence, the coefficient variation CV is employed to estimate the variability of the pixels instead of the variance. The local CV gives the edges, textures, and points a greater value than the pixels in homogeneous region. The parameter $b'_k(i)$ can be written as

$$b'_k(i) = f_1(CV_{\hat{x}_k}^2(i)) \quad (13)$$

where

$$f_1(x) = \frac{x}{(2x + 1)}. \quad (14)$$

From the numerical point of view, we can see that

- 1) the parameter $b'_k(i)$ that controls the speed of convergence is controlled by the CV (higher convergence in spatial details),
- 2) the objective of the function f_1 is to normalize $CV_{\hat{x}_k}^2(i)$ between 0 and 1 to ensure the convergence of the iterative method (numerical property i)

Fig. 1 shows the curve of $b'_k(i)$ as a function of $CV_{\hat{x}_k}(i)$ of (11) (dashed line). It can be seen that $0 < b'_k(i) < 0.5 < 1$. These low values demonstrate slow convergence in heterogeneous areas, which promoted the decrease in smoothness in

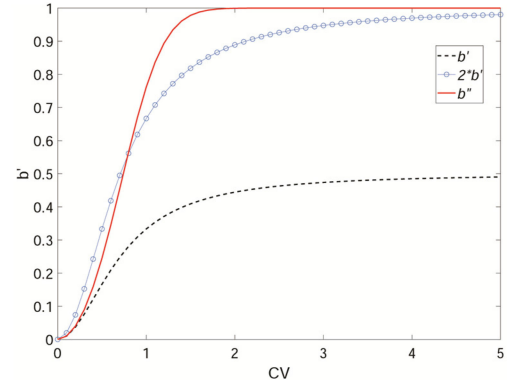


Fig. 1. Curves of b' as a function of CV.

homogeneous areas [29]–[31]. The use of $2 \times b'_k(i)$ alleviated this drawback (see circled line). However, it ensured slow convergence to the value 1. To address this problem, the authors proposed the following function:

$$f_2(x) = \tanh(x) \quad (15)$$

then

$$b''_k(i) = \tanh(CV_{\hat{x}_k}^2(i)) \quad (16)$$

where \tanh is the hyperbolic tangent used to ensure $0 < b''_k(i) < 1$. Fig. 1 plots the curve of $b''_k(i)$ as a function of $CV_{\hat{x}_k}(i)$ of (16) (solid line). It can be seen that $b''_k(i)$ turned to 1 rapidly, which addressed the numerical limitations of (11). However, in practice, due to the filtering action, the dynamic range of $CV_{\hat{x}_k}(i)$ is low, which implied difficulty to discriminate homogeneous and heterogeneous areas and slow convergence. To resolve this deficiency, the authors considered the following expression:

$$b''_k(i) = \tanh(CV_{\hat{x}_k}^2(i) CV_y^2(i)) \quad (17)$$

where $CV_y(i) \in [1, \infty]$ is the coefficient variation of the original pixel $y(i)$. It can be easily verified that in the homogeneous areas, $CV_{\hat{x}_k}(i) \approx 0$ and $CV_y(i) = 1$, so $b''_k(i) \approx 0$, whereas in heterogeneous areas, $CV_{\hat{x}_k}(i)$ is high, $CV_y(i)$ is higher, and $b''_k(i) \approx 1$. The main drawback of this solution is that the statistics are computed from the original speckled image. However, in many cases of SAR data (e.g., initially multilooked images), even in heterogeneous areas, $CV_y(i) < 1$ and $CV_{\hat{x}_k}(i) \ll 1$ so $b''_k(i) \ll 1$. In these cases, the iterative filtering ensured slow convergence to the original value. To resolve this problem, the expression inside \tanh in (17) has been normalized by the parameter C

$$b''_k(i) = \tanh\left(\frac{CV_{\hat{x}_k}^2(i) CV_y^2(i)}{C}\right). \quad (18)$$

Ideally, in homogeneous areas, when the process converge to $y(i)$, then

$$\frac{CV_{\hat{x}_k}^2(i) CV_y^2(i)}{C} = \frac{CV_y^2(i) CV_y^2(i)}{C} = \frac{1}{C(\text{ENL}_0(i))^2}. \quad (19)$$

By equalizing (17) and (18)

$$\frac{1}{C(\text{ENL}_0(i))^2} = 1 \quad (20)$$

then

$$C = \frac{1}{(\text{ENL}_0(i))^2} \quad (21)$$

where $\text{ENL}_0(i)$ is the equivalent number of looks of the original image $y(i)$ estimated in a homogenous area

$$\text{ENL}_0(i) = \frac{(\bar{y}(i))^2}{\text{var}(y(i))}. \quad (22)$$

In single look SAR data, $C = 1$, so that (17) and (18) are equivalent.

3) *Estimation of the Local Statistics*: The original IMMSE filter [29]–[31] adaptively estimates the parameter $b'_k(i)$ based on the local statistics using a square window. This choice reduced the complexity of the algorithm but some deficiencies can be noticed. For example, around boundaries between homogeneous and heterogeneous areas, the use of local square window overestimated the parameter $b'_k(i)$ in the homogeneous part (due to the presence of high variability in the window) and underestimated it in the heterogeneous part (due to the presence of homogeneous pixels in the window). Hence, pixels used for the estimation of the parameter $b'_k(i)$ are selected by analogy to the NL filtering principle. Each pixel in the search area gets a weight that comes from comparing its patch (neighborhood pixel that surrounds the candidate pixel) with the centered pixel patch. Then, and in order to reduce nonsimilar pixels, the authors considered only half pixels of the search area with the strongest patches. This strategy helped in reducing the nonhomogeneous pixels and increased the accuracy of estimating $\text{CV}_{\hat{x}}(i)$ and $\text{CV}_y(i)$.

III. EXPERIMENTAL RESULTS

To study the efficiency of the implemented filtering methods, simulated, airborne, and spaceborne SAR images were used (see Fig. 2). The authors considered the homogeneous image H to evaluate the ability of speckle filters on speckle reduction [see Fig. 2(a)]. The study also considered the heterogeneous area T to assess the ability of the proposed speckle filters on spatial detail preservation [see Fig. 2(b) and (c)]. In the second simulated image [see Fig. 2(d) and (e)], the authors simulated three speckled extended homogeneous areas Z1, Z2, and Z3. In addition, two types of deterministic targets (no speckle) characterized by high backscattering power have been introduced. The first represents six-point targets, and the second represents two lines. The test airborne SAR was the C-band hh image of Oberpfaffenhofen area, Germany acquired by ESAR Airborne sensor [see Fig. 2(f) and (g)]. The spaceborne data were the Sentinel 1 C-band vv SAR image of Palm Jumeirah, Dubai, UAE [see Fig. 2(h) and (i)].

A. Implemented Filters

- 1) *Boxcar* [2]: The value of the filtered pixel was the mean of pixels of a moving window $W = K \times K$.

- 2) *Improved Lee filter* [25], a moving window W_1 was applied. Pixels within the sigma range $(n_1y(i), n_1y(i))$ were included in computing $\hat{x}(i)$ in (2), where n_1, n_2 define the bounds of the sigma range.

- 3) *NLM filter* [8]. The NLM estimate \hat{x} can be defined in [32]

$$\hat{x}_{\text{NLM}}(i) = \sum_{j \in \Omega} w(i, j) y(j) \quad (23)$$

where Ω is the research area, the weight $w(i, j)$ denoted the similarity between the patches Λ_i and Λ_j

$$w(i, j) = \frac{1}{Z(i)} \exp\left(-\frac{d(\Lambda_i, \Lambda_j)}{h}\right) \quad (24)$$

where $Z(i)$ is the normalization factor, and h was the smoothing factor

$$Z(i) = \sum_j \exp\left(-\frac{d(\Lambda_i, \Lambda_j)}{h}\right). \quad (25)$$

For one look SAR speckle filtering, $d(\Lambda_i, \Lambda_j)$ can be expressed as [8]

$$d(\Lambda_i, \Lambda_j) = \sum_{m \in \Sigma} G(k) \frac{(z_i(m) - z_j(m))^2}{\bar{y}_i} \quad (26)$$

where Σ represent the set of pixels in the patch, \bar{y}_i was the mean value of y_i in the patch Λ_i , and G was the standard Gaussian kernel function.

- 4) *Practical implementation of the improved iterative filter*.

For a given SAR image y

- a) compute the parameter C in (18).
- b) compute \hat{x}_0 image by applying a filter ensuring high speckle reduction level. Since the ENL of the proposed filter decreases with respect to the increase in the iterations [29]–[31], to ensure high speckle reduction level, the speckle reduction level (i.e., ENL) of the original filter should be sufficiently high.

For a given pixel

- c) define the search window Ω_1 . From the selected pixels of the filtered image \hat{x}_0 , compute the similarity weights using (25) (search window Ω_1 , patch Σ_1). Then, discard half pixels having the lowest similarity coefficient values. Compute $\text{CV}_{\hat{x}}(i)$ using the retained pixels,
- d) from the selected pixel of the original image y , discard half pixels and compute $\text{CV}_y(i)$ using the same process in c),
- e) compute $b''_k(i)$ using (18),
- f) update the filtered pixel using (7),
- g) apply the process for all pixels of the image,
- h) repeat c)–g) N iterations. N is an input parameter introduced by the user to control the speckle reduction and spatial detail preservation.

- 5) *The basic IMMSE filter* [29]–[31].

The authors applied the iterative process using the boxcar filter as an initial filter. The parameter $b'_k(i)$ was given by (9). The variance was estimated using a square window W_2 .

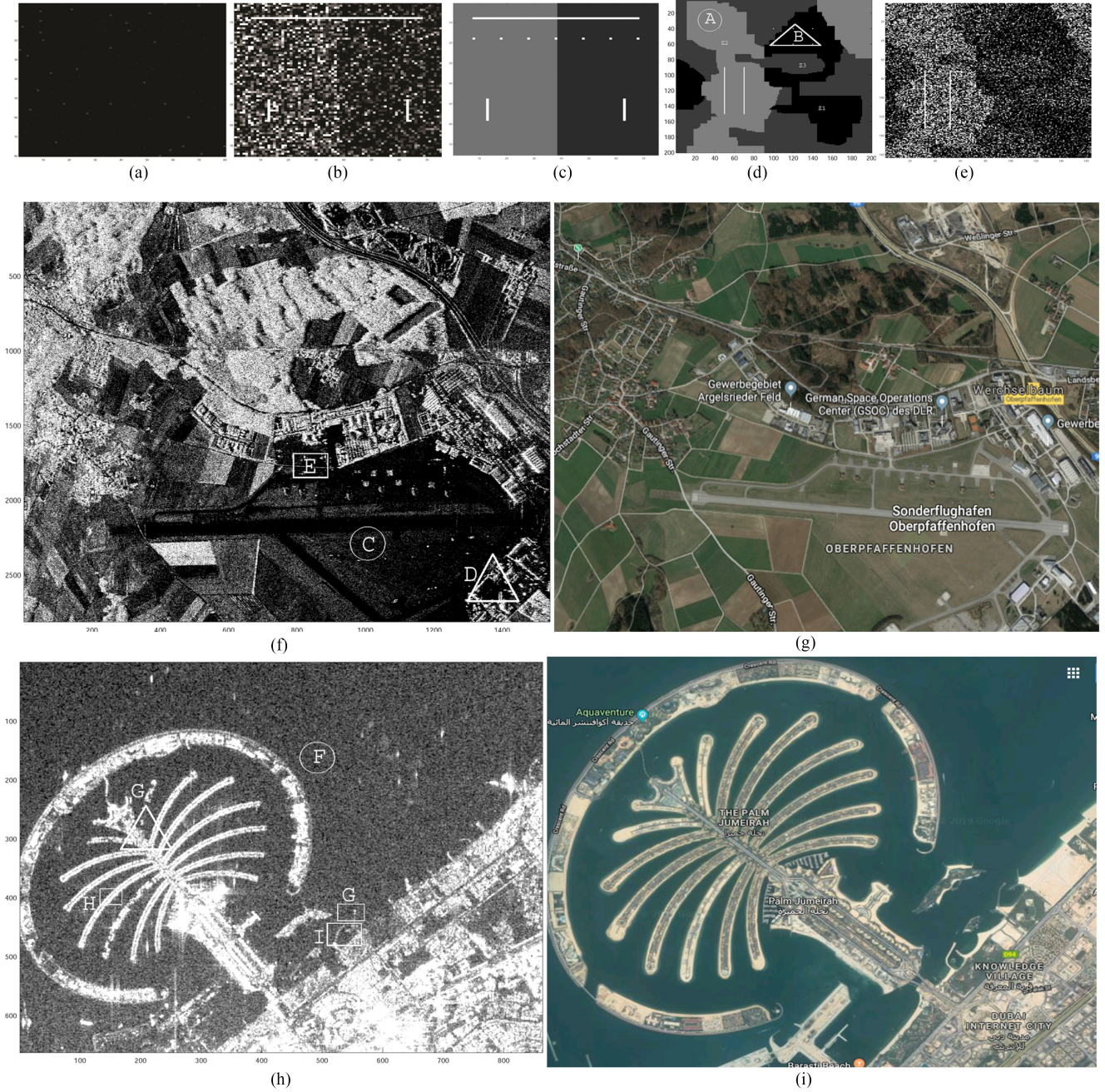


Fig. 2. (a) Simulated H zone ($\text{mean}(H) = 1$, $\text{var}(H) = 1$, $\text{ENL}_0 = 1$). (b) Heterogeneous T zone ($T(x, y) = 50$, where (x, y) are included in the introduced features), extended areas of mean 1 and 2. (c) Ground truth of T zone. (d) Ground truth GT of the simulated data 2 ($\text{GT}(Z1) = 0.09$, $\text{GT}(Z2) = 4.12$, $\text{GT}(Z3) = 3.46$, $\text{GT}(\text{lines}) = \text{GT}(\text{points}) = 100$). (e) Speckled image $\text{var}(Z_i) = Z_i^2$, $\text{ENL}_0 = 1$. (f) hh Oberpfaffenhofen area, $\text{ENL}_0 = 1$. (g) Ground truth [34]. (h) vv image Palm Jumeirah, $\text{ENL}_0 = 18.5$. (i) Ground truth [35]. Circular, triangular, and rectangular areas were used to assess speckle reduction (i.e., ENL), spatial detail preservation (i.e., MSE or EPD-ROA), and visual inspections, respectively.

B. Parameter Setting

Boxcar: $W = 9 \times 9$. Improved Lee filter: $W_1 = 11 \times 11$, $n_1 = 0.043$, $n_2 = 4.840$. NLM1 (normal use): $\Sigma = 7 \times 7$, $\Omega = 19 \times 19$, $h = 5$ (since $\text{ENL}_0 = 1$) for simulated and AirSAR data, whereas $h = 2$ for spaceborne data (since $\text{ENL}_0 = 18.5$). NLM2 (high-level smoothing action): $h = 2$ or 5 , $\Sigma = 11 \times 11$, $\Omega = 27 \times 27$. Original IMMSE: initial filter, boxcar $W = 9 \times 9$, $W_2 = 7 \times 7$. Improved iterative filter: initial filter, NLM1 or NLM2, $\Omega_1 = 7 \times 7$, $\Sigma_1 = 3 \times 3$.

C. Evaluation Criteria

In addition to visual inspections, quantitative parameters have been used to evaluate the performance of the studied filters. The authors chose the ENL to evaluate speckle reduction level

$$\text{ENL}(i) = \frac{(\bar{\hat{x}}(i))^2}{\text{var}(\hat{x}(i))}. \quad (27)$$

To illustrate the algorithm validity in spatial detail preserving of simulated images, the authors used the mean square error

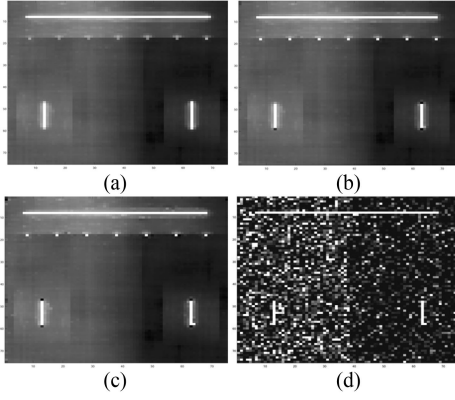


Fig. 3. Improved iterative1 filtered T images. (a) Initial filtered image NLM1. (b) $N = 1$. (c) $N = 3$. (d) $N = 100$.

(MSE). The MSE between the filtered and the noise free image is given by

$$\text{MSE}(i) = \frac{1}{M} \sum_{l=1}^M (\hat{x}(l) - x(l))^2 \quad (28)$$

where M is the number of processed pixels. For real SAR images, the authors used the edge preservation degree based on the ratio of averages (EPD-ROA) [33]. The EPD-ROA in horizontal direction is

$$\text{EPD} - \text{ROA}_H(i) = \frac{\sum_{m,n} |\hat{x}(m,n) / \hat{x}(m,n+1)|}{\sum_{m,n} |y(m,n) / y(m,n+1)|} \quad (29)$$

where m and n are the xy coordinates of the pixel in the selected zone, respectively. EPD-ROA_V is obtained by substituting in (29) the indexes $(m, n+1)$ by $(m+1, n)$. For the original image, $\text{EPD-ROA} = 1$. When the EPD-ROA is closer to one, it means better ability of spatial detail preservation.

D. Study of the Proposed Filter

Fig. 3 displays the filtered simulated images using the improved iterative filter for various iterations. It can be observed that the original filter (i.e., NLM1) degraded the spatial details partially. The application of the iterative filter, for one iteration, repaired this deficiency while preserving the high speckle filtering level in homogeneous areas. After three iterations, spatial details were affined. After 100 iterations, the process converged to the original image (i.e., y).

1) *Choice of Initial Filter*: Fig. 4 displays the filtered image using the improved iterative filter for various iterations using the boxcar as an initial filter. High blurring effects in the filtered images can be observed. Compared with Fig. 3, these blurring effects persisted more. Hence, initializing the iterative filter by the NLM provided better results than initializing by the boxcar.

2) *Choice of the Parameter b'* : Fig. 5(a) displays the ENL of zone H as a function of the MSE between the filtered image \hat{x} and the speckled image y of the zone T using the original and the improved iterative techniques. As expected, the filtering process converged to the original image (i.e., $\hat{x} = y$), where $\text{ENL} = 1$ and $\text{MSE} = 0$. It can be observed that the improved iterative gave

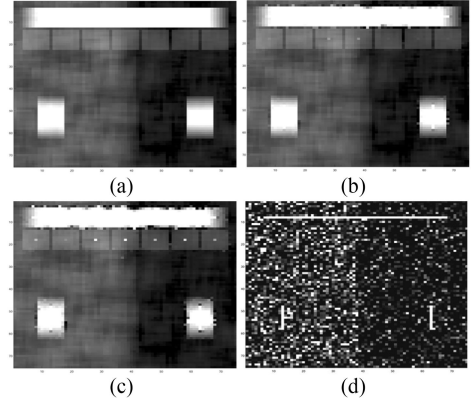


Fig. 4. Original IMMSE filtered T images. (a) Initial filtered image: boxcar 9×9 . (b) $N = 1$. (c) $N = 3$. (d) $N = 100$.

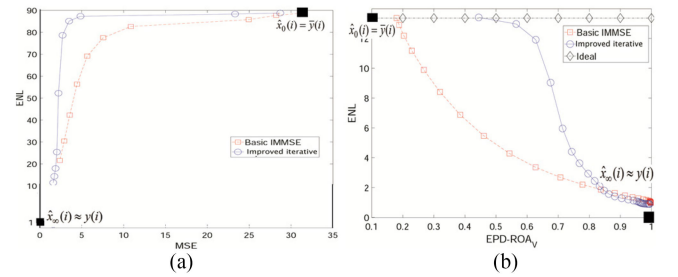


Fig. 5. Results of the IMMSE filter ($N = 10$). (a) ENL(H zone) versus MSE(T zone) of original and improved IMMSE. (b) ENL(A zone) versus EPD-ROA_V (B zone) of original and improved iterative methods. Both filters were initialized by boxcar $W = 9 \times 9$, $W_2 = 7 \times 7$. They differ from each other only by the expression of b' .

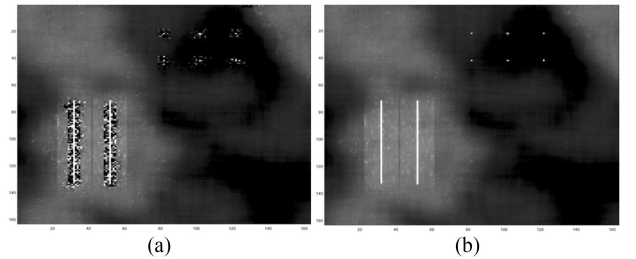


Fig. 6. (a) Improved iterative1 (local statistics estimated using a square window $W_2 = 7 \times 7$, $N = 3$). (b) Improved iterative1, $N = 3$.

better compromise between speckle reduction (higher ENL) and spatial detail preservation (lower MSE) than the original IMMSE. Fig. 5(b) shows the ENL of zone C as a function of the EPD-ROA_V of zone D. It can be observed that the filtering process converged to the original pixel value (i. e. $\hat{x} = y$) where $\text{ENL} = 1$ and $\text{EPD-ROA}_V = 1$. The improved iterative gave better compromise between speckle reduction (higher ENL) and spatial detail preservation (higher EPD-ROA) than the original version of the filter.

3) *Estimation of the Local Statistics*: Fig. 6(a) shows the filtered image using the improved iterative1 ($N = 1$). To estimate the local statistics, the authors used a square widow $W_2 = 7 \times 7$

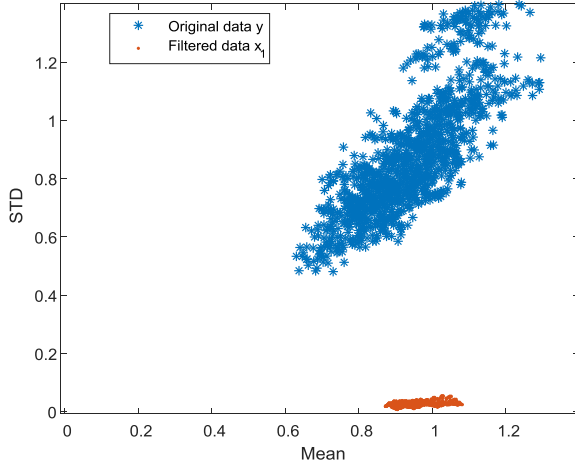


Fig. 7. Scatter plots of standard deviation versus mean using the simulated single look SAR image H [see Fig. 2(a)].

as the original IMMSE. It can be observed that lines and points are enhanced considerably. However, in the homogeneous areas around the lines and the points (which should be maintained smoothed), since the window contained pixels with high reflectivity (i.e., $b_k''(i) \approx 1$), the improved iterative filter converged to the original value too. By adopting the proposed strategy, this problem was mitigated [see Fig. 6(b)].

4) *Preservation of the Multiplicative Noise Model*: Fig. 7 displays scatter plots of standard deviation versus mean using a simulated single look HH SAR image [see Fig. 2(a)]. The linear dependence between the standard deviation versus the mean is noticeable for the original (i.e., $y(i)$) and the filtered (i.e., $\hat{x}_1(i)$) data. Hence, the multiplicative nature of the noise for the filtered data is still valid.

E. Comparison Using Simulated Data

Fig. 8 displays the performances of the studied filters on the simulated data. As expected, the boxcar filter provided good speckle reduction, but it degraded spatial details. On the other hand, the improved Lee filter preserved better spatial details at the cost of speckle reduction. The original IMMSE gave high speckle reduction level but altered the lines. The NLM1 provided a better balance between speckle reduction and detail preservation. The improved iterative1 in Fig. 8(f) maintained the high speckle reduction level of NLM1 and enhanced considerably the lines and the points. The NLM2 provided the highest speckle reduction level but compared with NLM1, it blurred the spatial details slightly [see Fig. 8(d)]. The improved iterative2 maintained the high speckle reduction level of NLM2 and corrected the blurring effects.

Table I displays the ENL of zone (A) and the MSE between the filtered and the cleaned image (zone B). It can be seen that the improved iterative1 maintained the high speckle reduction level as the initially applied filter (i.e., NLM1) and improved the spatial detail preservation ($\text{ENL} = 357 \approx 365$ and $\text{MSE} = 0.12 < 1.97$). The same results are observed concerning NLM2 and the improved iterative2 ($\text{ENL} = 560 \approx 575$ and $\text{MSE} =$

TABLE I
PERFORMANCES OF THE FILTERS USING SIMULATED DATA

	ENL	MSE
Boxcar 9×9	92	22.83
Improved Lee 11×11	5	7.07
NLM1	365	1.97
Improved iterative1, N=1	357	0.12
NLM2	575	15.43
Original IMMSE, N=5	82	21.98
Improved iterative2, N=3	560	0.15

The bold values represent the best values.

TABLE II
PERFORMANCES OF THE FILTERS USING AIRBORNE DATA

	ENL	EPD _H	EPD _V
Boxcar 9×9	13.68	0.1415	0.1441
Improved Lee 11×11	3.86	0.7567	0.7633
NLM1	20.89	0.1971	0.1993
Improved iterative1, N=1	17.38	0.2106	0.2142
NLM2	33.95	0.1827	0.1855
Original IMMSE N=5	11.73	0.1860	0.1875
Improved iterative2, N=2	24.76	0.2034	0.2075

The bold values represent the best values.

$0.15 < 15.43$). It is interesting to observe that the improved iterative2 performed better than NLM1 ($\text{ENL} = 560 > 365$ and $\text{MSE} = 0.15 < 1.97$).

F. Comparison Using AirSAR Data

Fig. 9 shows the filtered zone E of the AirSAR image. As for simulated data, the boxcar filter provided good speckle reduction while degrading spatial details. The original IMMSE increased the filtering performances. For NLM1 and NLM2, spatial details were improved considerably. Compared with NLM1, the blurring effect introduced by NLM2 was noticeable (see circled areas). The improved iterative1 and the improved iterative2 enhanced considerably spatial detail preservation. For example, the details showed by the circles, the squares, and the arrows were clearly enhanced. The improved Lee filter exhibited excellent spatial detail preservation.

Quantitative results in Table II confirmed visual inspections where the improved iterative filter maintained the high speckle reduction level of the initially applied filter and enhanced spatial details. It can be seen that the improved iterative2 outperformed NLM1 in terms of speckle reduction and spatial detail preservation. The improved Lee gave excellent spatial detail preservation at the cost of speckle filtering.

G. Comparison Using Spaceborne Data

Fig. 10 displays the performances of the studied filters on the Sentinel 1 SAR image of Palm Jumeirah in Dubai, UAE. Results showed that the boxcar gave weak spatial preservation since structures were considerably blurred. The improved Lee filter ensured better spatial detail preservation. The original IMMSE increased the filtering performances. For NLM1 and NLM2, spatial details were improved considerably. The improved iterative1 and improved iterative2 enhanced considerably the spatial

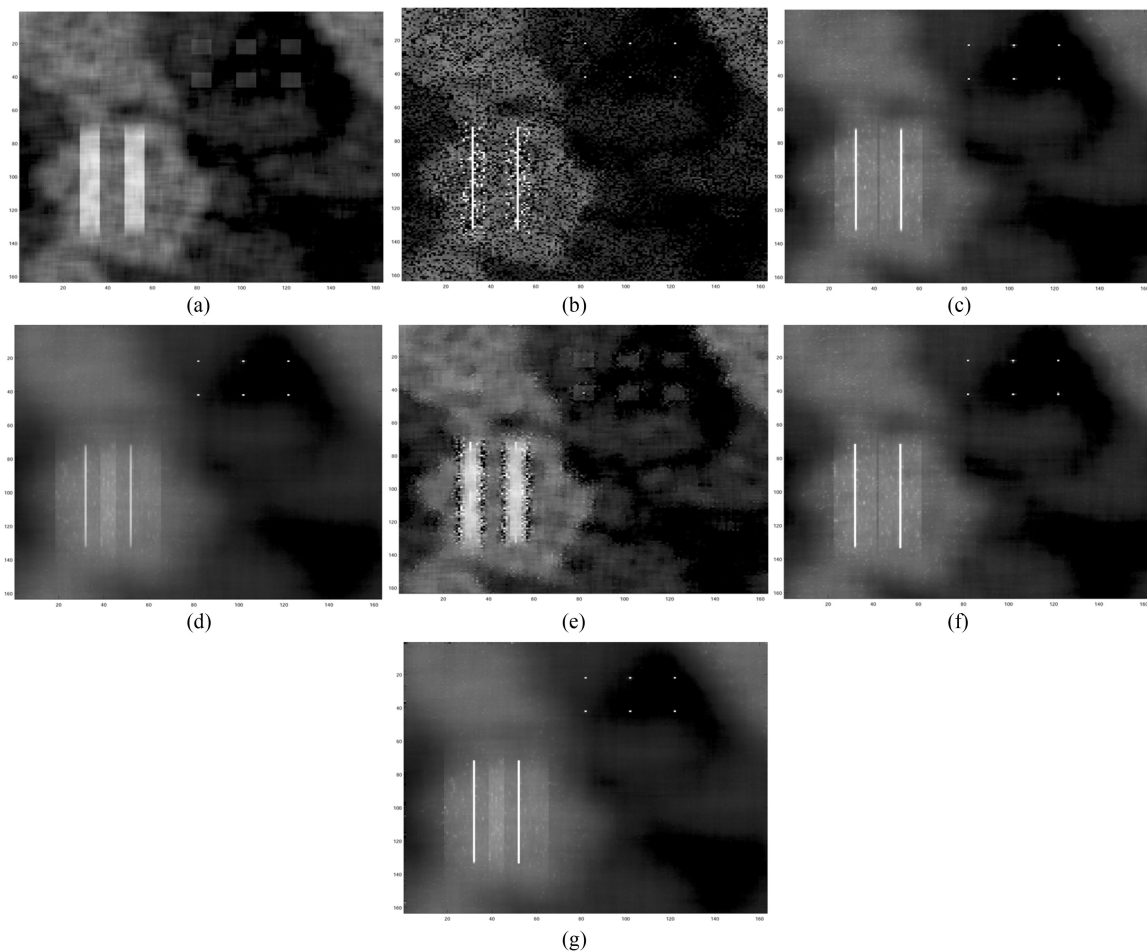


Fig. 8. Filtered simulated images. (a) Boxcar 9×9 . (b) Improved Lee 11×11 . (c) NLM1. (d) NLM2. (e) Original IMMSE, $N = 5$. (f) Improved iterative1, $N = 1$. (g) Improved iterative2, $N = 3$.

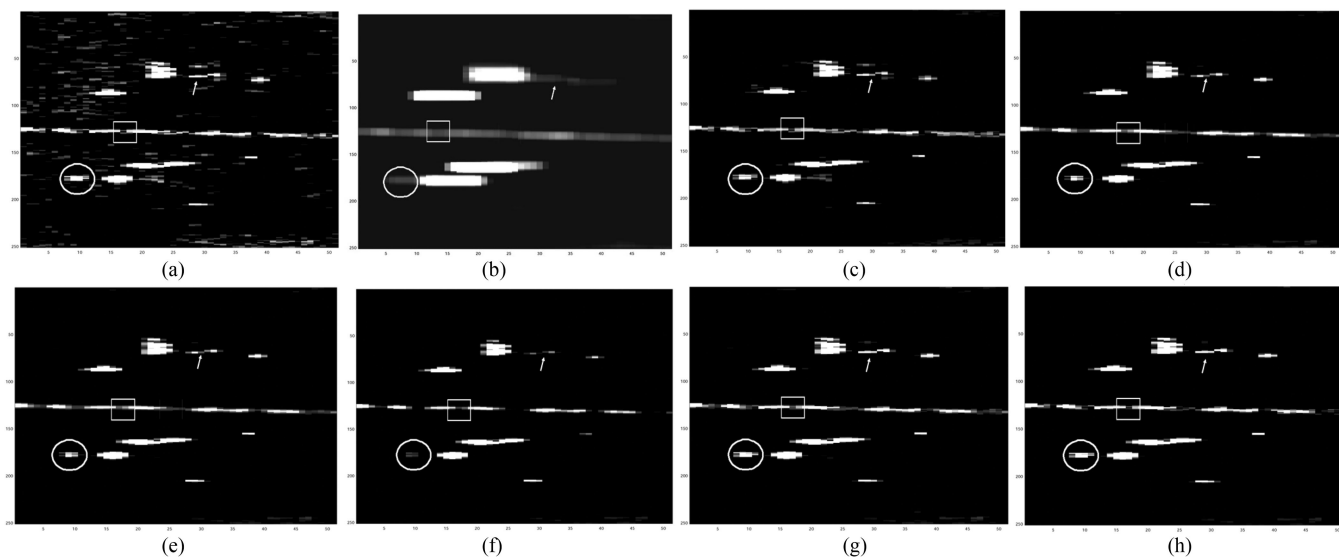


Fig. 9. Filtered E zone. (a) Original. (b) Boxcar 9×9 . (c) Improved Lee 11×11 . (d) NLM1. (e) NLM2. (f) Original IMMSE, $N = 5$. (g) Improved iterative1, $N = 1$. (h) Improved iterative2, $N = 2$.

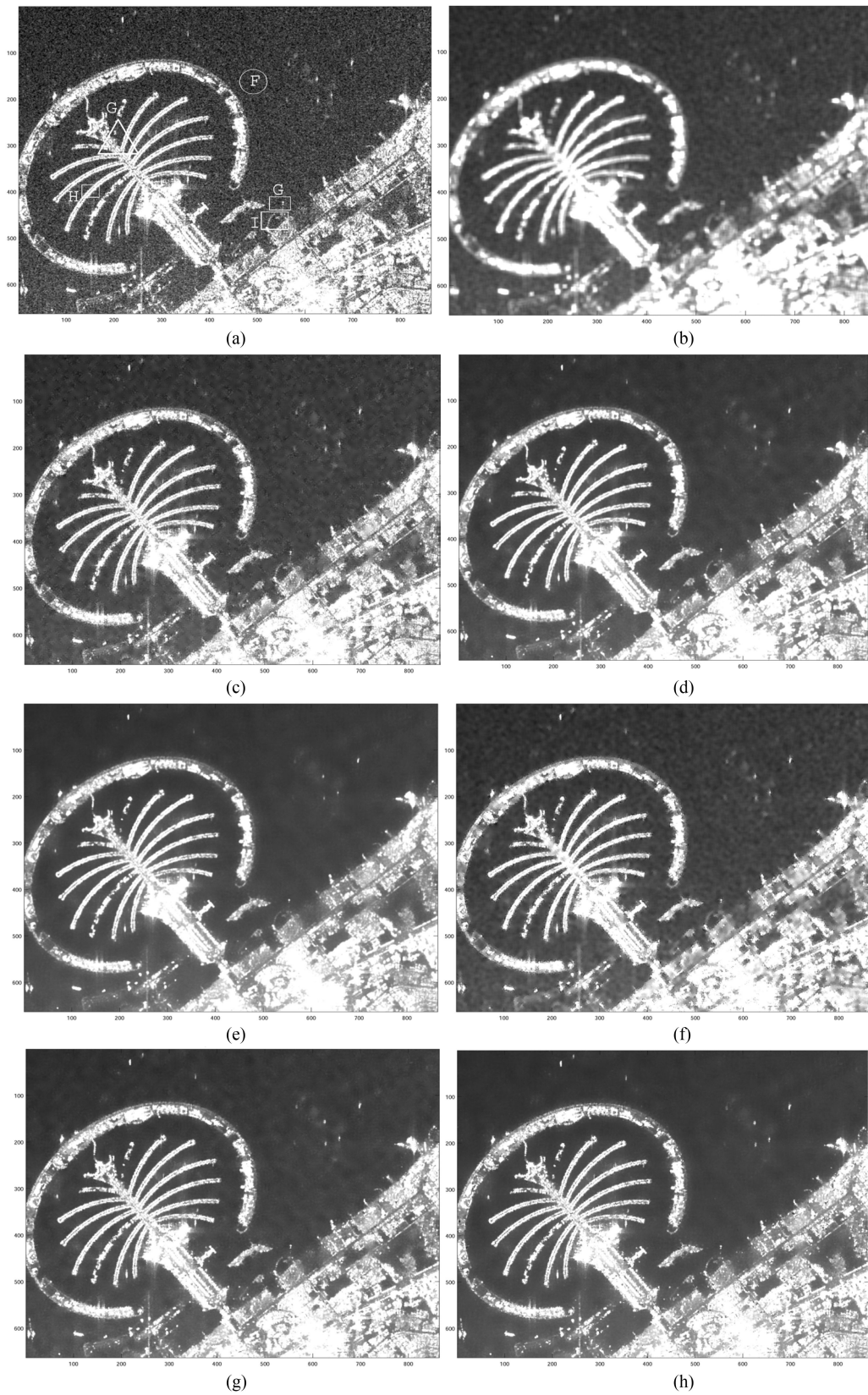


Fig. 10. Filtered Palm Jumeirah images. (a) Original. (b) Boxcar 9×9 . (c) Improved Lee 11×11 . (d) NLM1. (e) NLM2. (f) Original IMMSE, $N = 2$. (g) Improved iterative1, $N = 1$. (h) Improved iterative2, $N = 3$.

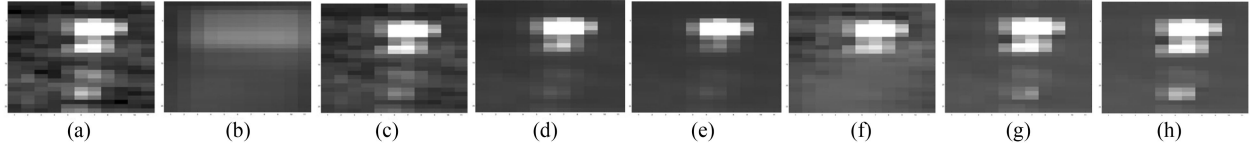


Fig. 11. Filtered G zone. (a) Original. (b) Boxcar 9×9 . (c) Improved Lee 11×11 . (d) NLM1. (e) NLM2. (f) Original IMMSE. (g) Improved IMMSE1. (h) Improved IMMSE2.

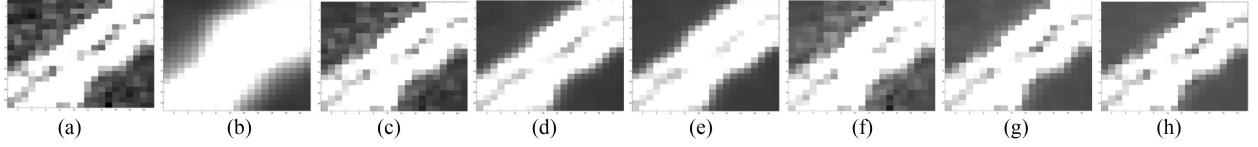


Fig. 12. Filtered H zone. (a) Original. (b) Boxcar 9×9 . (c) Improved Lee 11×11 . (d) NLM1. (e) NLM2. (f) Original IMMSE. (g) Improved iterative1. (h) Improved iterative2.

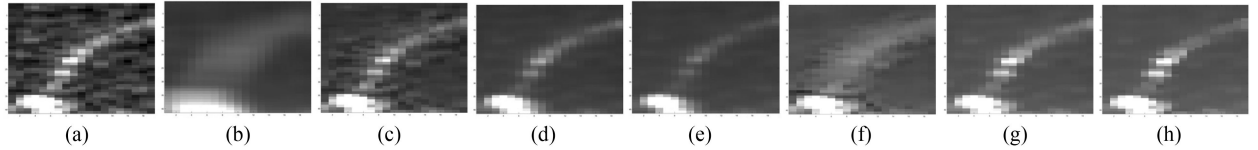


Fig. 13. Filtered I zone. (a) Original. (b) Boxcar 9×9 . (c) Improved Lee 11×11 . (d) NLM1. (e) NLM2. (f) Original IMMSE. (g) Improved iterative1. (h) Improved iterative2.

details while maintaining the high speckle reduction level of NLM1 and NLM2, respectively. To assess the spatial detail preservation more precisely, in Figs. 11–13 the zoomed filtered areas G, H, and I, respectively, are plotted. It can be observed from Fig. 11 that the point target that is completely smoothed by NLM2 and partially smoothed by NLM1 was enhanced using the improved iterative filter. Fig. 12 displays a part of a palm branch which is characterized by two rows of tall buildings separated by a road. The dark part is the sea [see ground truth in Fig. 2(e)]. It can be observed that the dark line is highly smoothed by NLM2 and partially smoothed by NLM1. This information was retrieved using the improved iterative filter. In addition, the proposed method increased the contrast between the sea and the buildings while maintaining the high speckle reduction level in the sea. The authors observed that in the sea zones, the original IMMSE converged to the original speckled values. This problem was surmounted using the improved iterative filter. In Fig. 13, zone I that represents a part of the port has been zoomed (see ground truth). The authors observed again that the boxcar smoothed the bright line. NLM1 and NLM2 gave better spatial detail preservation. For the proposed improved iterative filter, the line was considerably enhanced while preserving the high speckle reduction level of NLM1 and NLM2.

Quantitative results in Table III confirmed visual inspections where the improved iterative filter maintained the ENL of the initially applied filter and enhanced the EPD-ROA. It can be seen also that the improved iterative2 outperformed NLM1 in terms of speckle reduction ($ENL = 1602 > 791$) and spatial detail preservation ($EPD-ROA = 0.9816 > 0.9695$).

Fig. 14 displays the probability density functions (pdf) of the filtered homogeneous area F. It can be seen that the original

TABLE III
PERFORMANCES OF THE FILTERS USING SPACEBORNE DATA

	<i>ENL</i>	<i>EPD_H</i>	<i>EPD_V</i>
Boxcar 9×9	301	0.9350	0.9348
Improved Lee 11×11	158	0.9772	0.9770
NLM1	791	0.9695	0.9695
Improved iterative1, N=1	774	0.9787	0.9786
NLM2	1664	0.9631	0.9630
Original IMMSE N=2	287	0.9796	0.9795
Improved iterative2, N=3	1602	0.9818	0.9816

The bold values represent the best values.

IMMSE, the improved iterative1 and the improved iterative2 filters gave the same speckle reduction level as the initially applied filters, i.e., boxcar, NLM1 and NLM2, respectively, since their pdfs fit well.

H. Discussion

The performance of the improved iterative filter depended essentially on the choice of the initial filter, the choice of the parameter $b'_k(i)$, and the precise estimation of the local statistics. The improved iterative filter is not an independent filter since its performances depended on the choice of the initial filter. By initially applying a filter (e.g., the NLM1), the enhancement of SAR speckle denoising using the improved iterative filter can be achieved in two ways.

- 1) The normally applied filter (e.g., NLM1) can initialize the improved iterative. Then, by running a few iterations, the speckle reduction level was maintained, and the spatial detail preservation was enhanced.

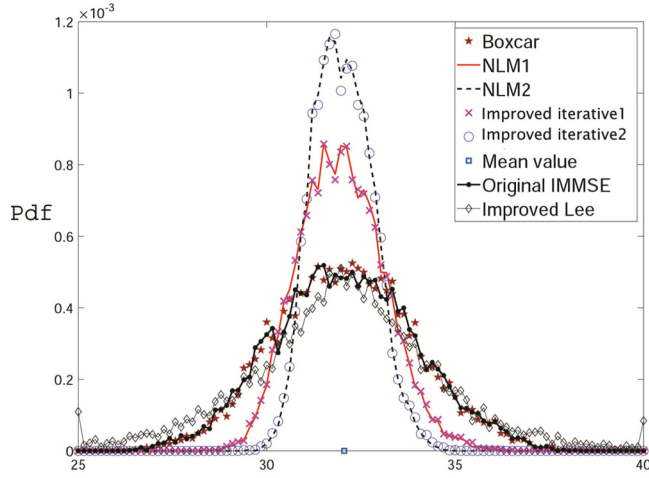


Fig. 14. pdf of the filtered homogeneous area F.

- 2) Initializing by higher speckle reduction level using the same filter (e.g., NLM2). Then, by running a few iterations, the improved iterative produced better filtering performances than the normally applied filter (e.g., NLM1) in terms of speckle reduction and spatial detail preservation.

In the improved iterative technique, the number of iterations is an input parameter defined by the user to control the smoothness degree. Low number of iterations promotes high-level speckle reduction, whereas a high number of iterations promotes high spatial detail preservation. By varying the number of iterations, the user could choose the best compromise between speckle reduction and spatial detail preservation depending on the scene variability of the original image. The development of an automatic stop criterion depending in the pixel statistics constitutes an interesting research topic.

In (18), the tanh function is applied to normalize the CVs between 0 and 1 (i.e., $0 < b'_k(i) = \tanh(\text{CV}) < 1$). Unless the process will diverge (i.e., $\hat{x}_\infty(i) = \infty$). $\hat{x}_\infty(i) = \infty$. Other functions ensuring better results could be naturally used. By choosing the tangent hyperbolic function in (13), the MMSE principle is disregarded. This important modification is proposed to overcome the numerical limitations of the IMMSE-based function (11).

This procedure is not specific to the NLM and could be extended to other filters.

It is important to mention that if initialized by the clean image x , the improved iterative preserved it. In fact, in homogeneous areas, $b''_k(i) = 0$, and in heterogeneous areas, $x(i) = y(i)$. So that, the second part of (7) is equal to zero.

The success of the improved iterative procedure is based on the choice of b'_k . In Fig. 5(b), the authors plotted the ENL versus EPD-ROA for the ideal case. The authors observed that the proposed parameter $b''_k(i)$ fits well the ideal case but needs further ameliorations. This issue will be deeply investigated in our future researches.

To estimate the local statistics of the pixels, the authors opted to preserve half pixels with strong patches in an NL search window. Unlike the NLM filtering, the objective here was not to select homogeneous pixels but the accurate estimation of

the local statistics (i.e., means and variances). For example, considering a homogeneous area containing a point target, when processing the homogeneous pixels, the point target was discarded. Then, the CV was more accurate and close to zero. On the other hand, for the point target, when discarding half of homogeneous pixels, the variance augmented which led to higher CV value. As a result, the homogeneous area and the point target had different statistics, which were not the case for a square window [see Figs. 6 and 12(f)]. This strategy is simple and need further improvements to affine local statistics estimation.

The computational complexity of the proposed method is $O(N \times N_x \times N_y \times N_1 \times N_2)$, where $N_x \times N_y$ is the size of the image, and $N_1 \times N_2$ is the dimension of the search area Ω_1 .

IV. CONCLUSION

In this article, the authors investigated the enhancement of SAR speckle filtering using the improved iterative filter. The effort was mainly focused on the choice of the parameter $b'_k(i)$, which traduced the variability of the processed pixels. Two improvements were proposed to estimate this parameter: Estimation the parameter $b'_k(i)$ using the coefficient variation rather than the variance and estimation of the statistics on an NL strategy instead of local square window. In addition, it has been demonstrated that the initial filtered image had a great impact on the filtering performances. Hence, by adequately choosing $b'_k(i)$ and the number of iterations, the proposed improved iterative filter can enhance the filtering performances of the initially applied filter. In future research, the authors will focus on optimizing the application of the proposed iterative filter to SAR and PolSAR speckle filtering.

APPENDIX

Let consider the function f

$$f(x) = b(y - x), x > 0 \quad (\text{A1})$$

where b and y are two positive reals. The root of the function f is

$$\alpha = y. \quad (\text{A2})$$

Our goal is to determine the root of the function f numerically

$$f(x) = 0 \Leftrightarrow x + b(y - x) = x \Leftrightarrow g(x) = x \quad (\text{A3})$$

where

$$g(x) = x + b(y - x). \quad (\text{A4})$$

It is possible from the fixed-point method formula $x_{k+1} = g(x_k) = x_k + b(y - x_k)$ starting with an initial approximating of x_0 and for $k \geq 0$, to get closer and closer approximations of a root α [36, p. 31]. To ensure the convergence of the sequence of approximations $\{x_k\}$, the function $g(x)$ should ensure the following condition [36, p. 32]:

$$|g'(x)| < 1, x > 0. \quad (\text{A5})$$

Then

$$0 < b < 2. \quad (\text{A6})$$

Since the sequence of approximations $\{x_k\}$ could be negative for $1 < b < 2$. Then

$$0 < b < 1. \quad (\text{A7})$$

ACKNOWLEDGMENT

The authors would like to thank German Aerospace Center (DLR) and European Space Agency (ESA) for providing the SAR data.

REFERENCES

- [1] A. Moreira, P. Prats-Iraola, M. Younis, G. Krieger, I. Hajnsek, and K. P. Papathanassiou, "A tutorial on synthetic aperture radar," *IEEE Geosci. Remote Sens. Mag.*, vol. 1, no. 1, pp. 6–43, Mar. 2013.
- [2] C. Oliver and S. Quegan, *Understanding Synthetic Aperture Radar Images*. Boston, MA, USA: Artech House, 1998.
- [3] Y. Hawwar and A. Reza, "Spatially adaptive multiplicative noise image denoising technique," *IEEE Trans. Image Process.*, vol. 11, no. 12, pp. 1397–1404, Dec. 2002.
- [4] F. Argenti and L. Alparone, "Speckle removal from SAR images in the undecimated wavelet domain," *IEEE Trans. Geosci. Remote Sens.*, vol. 40, no. 11, pp. 2363–2374, Nov. 2002.
- [5] L. Gagnon and A. Jouan, "Speckle filtering of SAR images: A comparative study between complex-wavelet-based and standard filters," in *Wavelet Applications in Signal and Image Processing V*, (Volume 3169 of SPIE Proceedings Series), A. Aldroubi, A. F. Laine, M. A. Unser Eds. Bellingham, WA, USA: SPIE, 1997, pp. 80–91.
- [6] E. Hervet, R. Fjortoft, P. Marthon, and A. Lopès, "Comparison of wavelet-based and statistical speckle filters," in *SAR Image Analysis, Modelling, and Techniques III*, (Volume 3497 of SPIE Proceedings Series), F. Posa, Ed. Bellingham, WA, USA: SPIE, 1998, pp. 43–54.
- [7] R. Grimson, N. S. Morandeira, and A. C. Frery, "Comparison of nonlocal means despeckling based on stochastic measures," in *Proc. IEEE Int. Geosci. Remote Sens. Symp.*, 2015, pp. 3091–3094.
- [8] H. Zhong, L. Lu, and L. Jiao, "Fast non-local lee filter for SAR image despeckling using directional projection," in *Proc. Int. Conf. Radar*, 2011, pp. 1600–1603.
- [9] S. Vitale, D. Cozzolino, G. Scarpa, L. Verdoliva, and G. Poggi, "Guided patchwise nonlocal SAR despeckling," *IEEE Trans. Geosci. Remote Sens.*, vol. 57, no. 9, pp. 6484–6498, Sep. 2019.
- [10] C. A. Deledalle, L. Denis, and F. Tupin, "Iterative weighted maximum likelihood denoising with probabilistic patch-based weights," *IEEE Trans. Image Process.*, vol. 18, no. 12, pp. 2661–2672, Dec. 2009.
- [11] Y. Zhao, J. G. Liu, B. Zhang, W. Hong, and Y. R. Wu, "Adaptive total variation regularization based SAR image despeckling and despeckling evaluation index," *IEEE Geosci. Remote Sens.*, vol. 53, no. 5, pp. 2765–2774, May 2015.
- [12] D. Gleich, M. Kseneman, and M. Datcu, "Despeckling of TerraSAR-X data using second-generation wavelets," *IEEE Geosci. Remote Sens. Lett.*, vol. 7, no. 1, pp. 68–72, Jan. 2010.
- [13] W. Zhang, F. Liu, L. Jiao, B. Hou, S. Wang, and R. Shang, "SAR image despeckling using edge detection and feature clustering in bandelet domain," *IEEE Geosci. Remote Sens. Lett.*, vol. 7, no. 1, pp. 131–135, Jan. 2010.
- [14] B. Hou, X. Zhang, X. Bu, and H. Feng, "SAR image despeckling based on onsubsampling shearlet transform," *IEEE J. Sel. Topics Appl. Earth Obs.*, vol. 5, no. 3, pp. 809–823, Jun. 2012.
- [15] H. Zhong, Y. Li, and L. Jiao, "SAR image despeckling using Bayesian nonlocal means filter with sigma preselection," *IEEE Geosci. Remote Sens. Lett.*, vol. 8, no. 4, pp. 809–813, Jul. 2011.
- [16] S. Parrilli, M. Poderico, C. V. Angelino, and L. Verdoliva, "A nonlocal SAR image denoising algorithm based on LLMMSE wavelet shrinkage," *IEEE Trans. Geosci. Remote Sens.*, vol. 50, no. 2, pp. 606–616, Feb. 2012.
- [17] D. Gragnaniello, G. Poggi, and L. Verdoliva, "Classification-based nonlocal SAR despeckling," in *Proc. Tyrrhenian Workshop Adv. Radar Remote Sens.*, 2012, pp. 121–125.
- [18] G. D. Martino, A. Di Simone, A. Iodice, G. Poggi, D. Riccio, and L. Verdoliva, "Scattering-based SARBM3D," *IEEE J. Sel. Topics Appl. Earth Obs.*, vol. 9, no. 6, pp. 809–823, Jun. 2016.
- [19] P. A. A. Penna and N. D. A. Mascarenhas, "SAR speckle nonlocal filtering with statistical modeling of haar wavelet coefficients and stochastic distances," *IEEE Trans. Geosci. Remote Sens.*, vol. 57, no. 9, pp. 7194–7208, Sep. 2019.
- [20] G. Vasile, E. Trounev, and J. S. Lee, "Intensity-driven adaptive-neighborhood technique for polarimetric and interferometric SAR parameters estimation," *IEEE Geosci. Remote Sens.*, vol. 44, no. 6, pp. 1906–1921, Jun. 2006.
- [21] J. S. Lee, "Digital image enhancement and noise filtering by use of local statistics," *IEEE Trans. Pattern Anal. Mach. Intell.*, vol. PAMI-2, no. 2, pp. 165–168, Mar. 1980.
- [22] J. S. Lee, "Digital image smoothing and the sigma filter," *Comput. Vis. Graph. Image Process.*, vol. 24, no. 2, pp. 255–269, Nov. 1983.
- [23] D. T. Kuan, A. A. Sawchuk, T. C. Strand, and P. Chavel, "Adaptive noise filtering for images with signal dependent noise," *IEEE Trans. Pattern Anal. Mach. Intell.*, vol. PAMI-7, no. 2, pp. 165–177, Mar. 1985.
- [24] V. S. Frost, J. A. Stiles, K. S. Shanmugan, and J. C. Holtzman, "A model for radar image and its application to adaptive digital filtering for multiplicative noise," *IEEE Trans. Pattern Anal. Mach. Intell.*, vol. PAMI-4, no. 2, pp. 175–186, Mar. 1982.
- [25] J. S. Lee, J.-H. Wen, T. L. Ainsworth, K.-S. Chen, and A. J. Chen, "Improved sigma filter for speckle filtering of SAR imagery," *IEEE Trans. Geosci. Remote Sens.*, vol. 47, no. 1, pp. 202–213, Jan. 2009.
- [26] J. S. Lee, T. L. Ainsworth, Y. Wang, and K. S. Chen, "Polarimetric SAR speckle filtering and the extended sigma filter," *IEEE Trans. Geosci. Remote Sens.*, vol. 53, no. 3, pp. 1150–1160, Mar. 2015.
- [27] E. Nezry, A. Lopes, and R. Touzi, "Detection of structural and textural features for SAR image filtering," in *Proc. IEEE Geosci. Remote Sens. Symp.*, 1991, vol. 3, pp. 2169–2172.
- [28] F. Argenti, T. Bianchi, and L. Alparone, "Multiresolution MAP despeckling of SAR images based on locally adaptive generalized Gaussian pdf modeling," *IEEE Trans. Image Process.*, vol. 15, no. 11, pp. 3385–3399, Nov. 2006.
- [29] M. Yahia, T. Hamrouni, and R. Abdelfattah, "SAR speckle denoising using iterative filter," in *Proc. Int. Geosci. Remote Sens. Symp.*, 2017, pp. 1756–1760.
- [30] S. Fatnassi, M. Yahia, and R. Abdelfattah, "SAR speckle filtering using hybrid non local and iterative MMSE filters," in *Proc. Int. Geosci. Remote Sens. Symp.*, 2019, pp. 1781–1784.
- [31] T. Hamrouni, M. Yahia, and R. Abdelfattah, "PolSAR speckle filtering using iterative MMSE," in *Proc. Int. Geosci. Remote Sens. Symp.*, 2018, pp. 637–640.
- [32] A. Buades, B. Coll, and J. M. Morel, "A non-local algorithm for image denoising," in *Proc. IEEE Comput. Vis. Pattern Recognit.*, Jun. 2005, vol. 2, pp. 60–65.
- [33] H. Feng, B. Hou, and M. Gong, "SAR image despeckling based on local homogeneous-region segmentation by using pixel-relativity measurement," *IEEE Trans. Geosci. Remote Sens.*, vol. 49, no. 7, pp. 2724–2737, Jul. 2011.
- [34] Ground truth Oberpfaffenhofen area, 2019. [Online]. Available: <https://www.google.com/maps/@25.1175391,55.1264783,2987m/data=!3m1!1e3>
- [35] Ground truth Palm Jumeirah, 2019. [Online]. Available: <https://www.google.com/maps/@48.0835617,11.2773744,2796a,35y,312.19h/data=!3m1!1e3>
- [36] S. S. Sastry, *Introductory Methods of Numerical Analysis*. New Delhi, India: PHP Learning Private Limited, 2012.



Mohamed Yahia received the B.Sc. degree from the Higher School of Sciences and Techniques, Tunis, Tunisia, in 2000, the M.Sc. degree from the Higher School of Communication, Tunis, Tunisia, in 2002, the Ph.D. degree in telecommunication engineering conjointly from the National Engineering School of Gabes (NESG), Tunisia, the Ecole Nationale Supérieure d'Electrotechnique, d'Electronique, d'Informatique, d'Hydraulique et des Télécommunications (ENSEEHT), Toulouse, France, in 2010, and the Habilitation degree in telecommunications from the University of Gabes, Tunisia, in 2017.

In 2018, he was an Associate Professor with NESG. Since 2019, he has been a Visiting Researcher with the American University of Sharjah. His current research interests include analysis of polarimetric SAR images and numerical methods in electromagnetism.



Tarig Ali received the B.S. (hons.) degree from the University of Khartoum, Sudan, in 1993, and the M.S. and Ph.D. degrees from Ohio State University, USA, in 1999 and 2003, respectively.

He is an Associate Professor with the American University of Sharjah. His research interests include GIScience, LiDAR mapping, mobile and Internet-based GIS, coastal mapping and GIS, applications of GIS/remote sensing in environmental & transportation engineering, wide-area GPS networks, and infrastructure monitoring/surveillance.



Mohammad Maruf Mortula received the B.Sc. degree from the Bangladesh University of Engineering and Technology, Bangladesh, in 2000, the M.Sc. and Ph.D. degrees from Dalhousie University, Canada, in 2002 and 2006, respectively.

Since 2018, he has been a Full Professor with the American University of Sharjah. His research interests include water and wastewater treatment, recycling of solid waste management, water quality management in coastal water, and water infrastructure management.



Riadh Abdelfattah (Senior Member, IEEE) received the Engineer degree from the Telecommunication Engineering School of Tunis, Tunisia, in 1995, the master's (DEA) and the Ph.D. degrees in electrical engineering from the Ecole Nationale Ingénieurs de Tunis in 1995 and 2000, respectively, and le Diplôme de l'Habilitation Universitaire degree from the Higher School of Communications for Engineers (SUP'COM), University of Carthage, Tunisia, in 2008.

Since December 2017, he has been the Vice-President of the University of Carthage, where he is also a Professor with the SUP'COM. He is an Associate Researcher with the Department ITI, IMT-Atlantique, Brest, France. Between 2000 and 2002, he was a Postdoctoral Researcher with the Ecole Nationale des Télécommunications, Paris, France, consecutively with the Department TSI and then with the Department COMELEC. He has authored and coauthored more than 70 journal papers, conference papers, and book chapters. His main research interests include interferometric radar imaging, multitemporal and multiscale image analysis, desertification, flooding and soil salinity mapping from remote sensed data, and SAR-nanosatellite development.

Dr. Abdelfattah was an Elected Member at the scientific council of the Agence Universitaire de la Francophonie (AUF), from 2016 to 2018, and a Member of the "Commission Régionale des Experts" of AUF. During 2011–2017, he was an Elected Member at the University Council of Carthage. He is cochairing the Mediterranean and MENA Geoscience and Remote Sensing Symposium to be held in Tunis in March 2020. He is a founding member of the Research Unit in Satellite Imagery and its Applications in January 2004 (2004–2011) and a founding member of the Communication, Signal and Image Laboratory, SUP'COM, in November 2011. He served as a Member of the Executive Committee of the IEEE Tunisia Section during 2013–2015.



Samy El Mahdy received the B.Sc. degree in geology from Ain Shams University, Egypt, in 1987, the M.Sc. degree in remote sensing and the Ph.D. degree in the application of GIS and geomatics engineering in geotechnical engineering from the University of Putra, Malaysia, in 2006 and 2013, respectively.

He is a Geospatial Scientist with the American University of Sharjah. He has authored or coauthored more than 35 research articles in journals and conference proceedings. He has more than 25 years of experience in research with particular interest in quantitative remote sensing, GIS and geosciences.

Dr. El Mahdy received the Gold Medal from the Malaysian National Space Agency in 2011 and won the first place in the Rashid Bin Humaid Award for Scientific Research in 2017.



Nuwanthi Sashipraba Arampola received the B.Sc. (hons.) degree in surveying science (specialization in photogrammetry and remote sensing) from the Faculty of Geomatics, Sabaragamuwa University of Sri Lanka, in 2017.

She is a Visiting Research Scholar with the American University of Sharjah, UAE. Her research interests include Optical and RADAR (sentinel 1) Satellite Remote Sensing for flood, land cover, land surface, marine, and coastal applications, GIS applications and spatial modeling, Spatio-Temporal analysis on

earth and its environment, and Geostatistical modelling and predicting an assessing triggers for the tree mortality.